

# Hybrid symmetry class topological insulators

Sanjib Kumar Das<sup>1</sup> and Bitan Roy<sup>1</sup>

<sup>1</sup>*Department of Physics, Lehigh University, Bethlehem, Pennsylvania, 18015, USA*

(Dated: May 26, 2023)

Traditional topological materials belong to different Altland-Zirnbauer symmetry classes (AZSCs) depending on their non-spatial symmetries. Here we introduce the notion of hybrid symmetry class topological insulators (HSCTIs): A fusion of two different AZSC topological insulators (TIs) such that they occupy orthogonal Cartesian hyperplanes and their universal massive Dirac Hamiltonian mutually anticommute. The boundaries of HSCTIs can also harbor TIs, typically affiliated with an AZSC different from the parent ones. As such, a fusion between planar quantum spin Hall and vertical Su-Schrieffer-Heeger insulators gives birth to a three-dimensional HSCTI, accommodating quantum anomalous Hall insulators and quantized Hall conductivity on the top and bottom surfaces. We extend this construction to encompass crystalline HSCTI and topological superconductors, and beyond three dimensions. Possible (meta)material platforms to harness HSCTIs are discussed.

*Introduction.* Twenty first century physics thus far is heavily influenced by the topological classification of quantum materials [1–10]. It roots back in the discovery of quantum Hall states in the 1980s [11–13]. Over the time, topological insulators (TIs), featuring insulating bulk but gapless boundaries via a bulk-boundary correspondence, emerged as the most prominent representative of topological phases of matter. It turned out that they can be grouped into ten Altland-Zirnbauer symmetry classes (AZSCs), depending on their non-spatial symmetries (time-reversal, particle-hole and sublattice or chiral) [14–16]. AZSCs also encompass thermal topological insulators or superconductors [17–19]. Subsequent inclusion of crystal symmetries in the classification scheme immensely diversified the landscape of topological phases that ultimately gave birth to topological quantum chemistry, nowadays routinely employed to identify topological crystals in nature [20–28]. In this realm, the following quest fuels our current venture. *Can a hybridization (defined shortly) between two topological insulators from different AZSCs foster (possibly new) topology?*

We offer an affirmative answer to this question by introducing the notion of hybrid symmetry class topological insulators (HSCTIs). Notice that all TIs (electrical or thermal) from AZSCs can be modeled by Dirac Hamiltonian with a momentum-dependent Wilson-Dirac mass [15, 16], manifesting band inversion around a time reversal invariant momentum (TRIM) point in the Brillouin zone (BZ). A hybridization between two TIs from distinct AZSCs occurs when they occupy orthogonal Cartesian hyperplanes and their band-inverted massive Dirac Hamiltonian mutually anticommute. We show that the resulting HSCTI can nurture emergent topology.

The construction of HSCTIs is showcased here from its simplest possible incarnation in three dimensions, stemming from the hybridization between a two-dimensional (2D)  $xy$  planar quantum spin Hall insulator (QSHI) and a one-dimensional (1D)  $z$ -directional Su-Schrieffer-Heeger insulator (SSHI). The top and the bottom surfaces of the resulting three-dimensional (3D) HSCTI then support

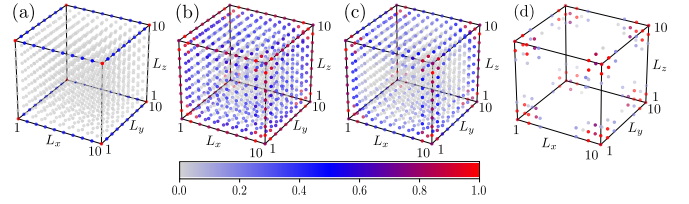


FIG. 1. Normalized local density of states for (a) surface localized chiral edge states of HSCTI, (b) surface states of a first-order TI [29], (c)  $z$ -directional hinge and  $xy$  surface state of a second-order TI [30], and (d) eight corner modes of a third-order TI [31, 32]. The lattice models for (b), (c) and (d) are discussed in the Supplemental Material [33].

1D edge states of opposite chiralities, producing integer quantized Hall conductivity (in units of  $e^2/h$ ) of opposite signs on these two surfaces. Thus, a 3D HSCTI is distinct from the presently known strong  $Z_2$  and higher-order TIs respectively supporting gapless surface states on six faces of a cube (first-order) [29] and  $z$ -directional hinge modes along with  $xy$  surface states (second-order) [30] or eight corner modes (third-order) [31–33]. See Fig. 1. It is also distinct from 3D axion insulators [34–36], displaying a non-quantized surface Hall conductivity.

*3D HSCTI.* To arrive at the model Hamiltonian for the 3D HSCTI, consider first the Bloch Hamiltonian [5]

$$h_{\text{QSHI}}^{xy} = d_1(\mathbf{k})\Gamma_1 + d_2(\mathbf{k})\Gamma_2 + d_3(\mathbf{k})\Gamma_3. \quad (1)$$

The components of the  $\mathbf{d}$ -vector for now are chosen to be  $d_1(\mathbf{k}) = t \sin(k_x a)$ ,  $d_2(\mathbf{k}) = t \sin(k_y a)$  and  $d_3(\mathbf{k}) = m_0 + t_0[\cos(k_x a) + \cos(k_y a)]$ . Here  $a$  is the lattice spacing. The hopping parameter  $t$  is set to be unity. Mutually anti-commuting Hermitian  $\Gamma$  matrices are  $\Gamma_j = \sigma_3 \tau_j$  for  $j = 1, 2, 3$ . The Pauli matrices  $\{\tau_\mu\}$  ( $\{\sigma_\mu\}$ ) operate on the orbital (spin) degrees of freedom with  $\mu = 0, \dots, 3$ . Then the above model describes a QSHI in the  $xy$  plane within the parameter regime  $-2 < m_0/t_0 < 2$ , featuring counter-propagating helical edge modes for opposite spin projections (class AII). When topological  $h_{\text{QSHI}}^{xy}$  is

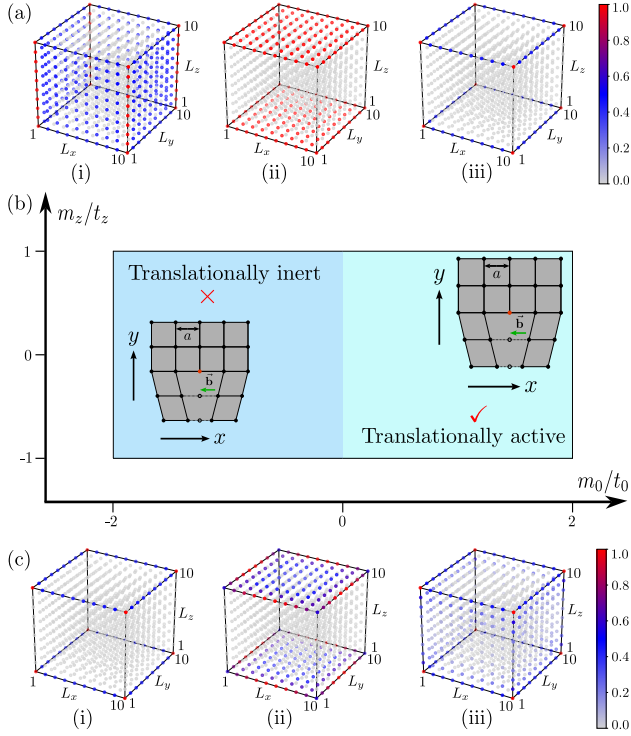


FIG. 2. (a) Normalized local density of states for the (i) edge modes of decoupled QSHIs for  $m_0/t_0 = 1$ , (ii) endpoint modes for decoupled SSHIs for  $m_z/t_z = 0$ , and (iii) chiral edge modes of HSC TI for  $m_0/t_0 = 1$  and  $m_z/t_z = 0$  [same as Fig. 1(a)]. (b) Phase diagram of HSC TI in the  $(m_0/t_0, m_z/t_z)$  plane. The translationally active (inert) phase supports (is devoid of) dislocation defect modes. (c) Melting of (i) chiral edge modes [same as (aiii)] by tuning (ii)  $m_0/t_0$  to 1.75 for a fixed  $m_z/t_z = 0$  and (iii)  $m_z/t_z$  to 0.75 for fixed  $m_0/t_0 = 1.0$ .

implemented on a 3D cubic lattice without any tunneling in the  $z$  direction, it supports a column of edge modes occupying the  $xz$  and  $yz$  planes. See Fig. 2(ai).

Next consider a second Bloch Hamiltonian [37–39]

$$h_{\text{SSH}}^z = d_4(\mathbf{k})\Gamma_4 + d_5(\mathbf{k})\Gamma_5, \quad (2)$$

where  $d_4(\mathbf{k}) = t_1 \sin(k_z a)$  and  $d_5(\mathbf{k}) = m_z + t_z \cos(k_z a)$ . We set  $t_1 = 1$ . If  $\Gamma_4$  and  $\Gamma_5$  are anticommuting Pauli matrices,  $h_{\text{SSH}}^z$  describes a  $z$ -directional SSHI (class BDI). Within the parameter range  $|m_z/t_z| < 1$ , it supports topological zero energy modes, localized at its two ends. If we place such  $z$ -directional topological SSHIs on the sites of a square lattice on the  $xy$  plane without any coupling between them, the resulting system features a collection of end point zero energy modes that occupies the entire top and bottom  $xy$  surfaces. See Fig. 2(aii).

With the ingredients in hand, we now announce the Bloch Hamiltonian for a 3D HSC TI, given by

$$h_{\text{HSC TI}}^{3D} = h_{\text{QSH}}^{xy} + h_{\text{SSH}}^z, \quad (3)$$

where now  $\Gamma_4 = \sigma_1\tau_0$  and  $\Gamma_5 = \sigma_2\tau_0$ , that together with  $\Gamma_1, \Gamma_2$  and  $\Gamma_3$  constitute a set of five four-

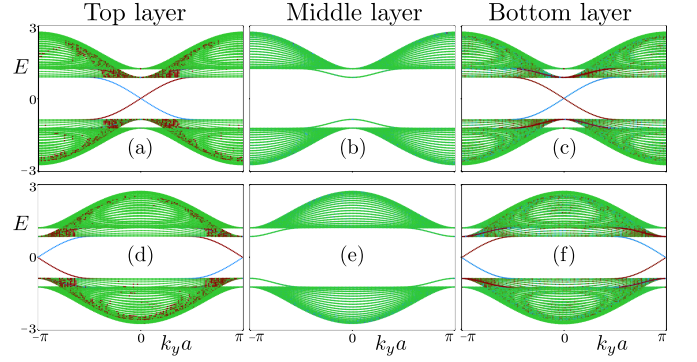


FIG. 3. Layer resolved (in the  $z$  direction) band structure of a 3D HSC TI with  $k_y$  as a good quantum number and  $L_x = L_z = 20$  for  $m_z/t_z = 0$ , and  $m_0/t_0 = -1.0$  (upper panel) and  $m_0/t_0 = 1.0$  (lower panel). Here blue (brown) and green indicate states localized near the left (right) edge and in the bulk of the system. Therefore, the top and bottom layers support counter-propagating chiral edge modes, while other layers are devoid of gapless states (such as the middle one).

component Hermitian matrices, satisfying the Clifford algebra  $\{\Gamma_j, \Gamma_k\} = 2\delta_{jk}$ . Here  $\delta_{jk}$  is the Kronecker delta function. Thus,  $h_{\text{QSH}}^{xy}$  and  $h_{\text{SSH}}^z$  anticommute with each other (hybridization). The  $z$ -directional SSHI acts as a mass for the edge modes of the  $xy$  planar QSHI and vice versa. Then one component of  $h_{\text{HSC TI}}^{3D}$  gaps out the topological modes of the other, except where both of them support topological gapless modes, namely along the edges on the top and bottom surfaces. See Fig. 2(aiii). But, the bulk is an insulator. Therefore, we realize a 3D TI by hybridizing two TIs, living on orthogonal Cartesian hyperplanes and belonging to different AZSCs, that manifests a bulk-boundary correspondence: a HSC TI.

**Symmetries.** The model Hamiltonian for a 3D HSC TI  $h_{\text{HSC TI}}^{3D}$  breaks (1) the time-reversal ( $\mathcal{T}$ ) symmetry generated by  $\mathcal{T} = \sigma_2\tau_1\mathcal{K}$ , where  $\mathcal{K}$  is the complex conjugation, and (2) the parity ( $\mathcal{P}$ ) symmetry, generated by  $\Gamma_3$  with  $\mathcal{P} : \mathbf{k} \rightarrow -\mathbf{k}$ . But, it preserves the composite  $\mathcal{PT}$  symmetry that guarantees a two-fold degeneracy of the conduction and valence bands of  $h_{\text{HSC TI}}^{3D}$ , respectively determined by the eigenspectra  $\pm E(\mathbf{k})$ , where  $E(\mathbf{k}) = [\alpha(\mathbf{k})]^{1/2}$  and  $\alpha(\mathbf{k}) = d_1^2(\mathbf{k}) + \dots + d_5^2(\mathbf{k})$ .

Notice that  $h_{\text{HSC TI}}^{3D}$ , involving all *five* mutually anticommuting four-component Hermitian  $\Gamma$  matrices, does not possess the sublattice or chiral symmetry, generated by a unitary operator that anticommutes with it. Rather it enjoys an anti-unitary particle-hole symmetry, generated by  $\mathcal{A} = \sigma_0\tau_1\mathcal{K}$ , such that  $\{h_{\text{HSC TI}}^{3D}, \mathcal{A}\} = 0$  [40].

**Phase diagram.** In the  $(m_0/t_0, m_z/t_z)$  plane, a 3D HSC TI occupies a rectangular region bounded by  $|m_0/t_0| < 2$  and  $|m_z/t_z| < 1$ , where both the parent insulators are topological. See Fig. 2(b). Furthermore, this topological regime fragments into two sectors for  $-2 < m_0/t_0 < 0$  and  $0 < m_0/t_0 < 2$ , when the band

inversion of the underlying QSHI takes place near the  $\Gamma = (0,0)$  point ( $\Gamma$  phase) and  $M = (1,1)\pi/a$  point ( $M$  phase) of a 2D square lattice BZ, respectively [41]. Dislocation lattice defects are instrumental in distinguishing these two regimes about which more in a moment.

A HSCTI can be pushed out of the topological regime by tuning  $m_0/t_0$  or  $m_z/t_z$  or both. As the ratio  $m_0/t_0$  is tuned from the topological toward trivial regime, the edge modes living on the opposite sides of the top or bottom surfaces start to hybridize, as shown in Fig. 2(cii). By contrast, as we tune  $m_z/t_z$  out of the topological regime the edge modes residing on the top and bottom surfaces mix through four side surfaces of the cube, as shown in Fig. 2(ciii). Once the system becomes a trivial insulator, there is no topological boundary modes.

*Bulk-boundary correspondence.* The nature of the edge modes of the 3D HSCTI on the top and bottom surfaces can be anchored from the effective surface Hamiltonian. For simplicity, we consider a semi-infinite system with a hard-wall boundary at  $z = 0$ . When the region  $z < 0$  ( $z > 0$ ) is occupied by HSCTI (vacuum), the surface at  $z = 0$  represents the top one. By contrast, when the region  $z > 0$  ( $z < 0$ ) is occupied by HSCTI (vacuum) the  $z = 0$  surface corresponds to the bottom one. A straightforward calculation, shown in the Supplemental Material [33], leads to the following surface Hamiltonian

$$H_{\text{surface}}^{\text{top/bottom}} = d_1(\mathbf{k})\beta_1 + d_2(\mathbf{k})\beta_1 \mp d_3(\mathbf{k})\beta_3, \quad (4)$$

where  $\mathbf{k} = (k_x, k_y)$ . The newly introduced Pauli matrices  $\{\beta_\mu\}$  operate on the space of two zero energy top/bottom surface states. With the chosen form of the  $\mathbf{d}$ -vector, this Hamiltonian mimics the Qi-Wu-Zhang model for a square lattice quantum anomalous Hall insulator (QAHI) [42]. Therefore, the top and bottom surfaces of the 3D HSCTI harbor two-dimensional QAHI with opposite first Chern numbers. On each surface the  $\mathcal{T}$  symmetry is broken. In addition, they also break the  $\mathcal{P}$  symmetry, under which the top and bottom surfaces switch, as they foster QAHI of opposite Chern numbers. Boundaries of a 3D HSCTI this way manifest the conserved composite  $\mathcal{PT}$  symmetry of its bulk. Finally notice that  $H_{\text{surface}}^{\text{top/bottom}}$  belongs to class A, a distinct AZSC from its parent QSHI (class AII) and SSHI (class BDI).

As the top and bottom surfaces host QAHI of opposite Chern numbers, they feature counter-propagating chiral edge states. See Fig. 3. We consider a semi-infinite system with  $k_y$  as good quantum number, and finite extensions in the  $x$  and  $z$  directions with open boundary conditions. For every  $z$ , we compute the band structure of a 3D HSCTI. Inside the topological regime of HSCTI, the top and bottom surfaces indeed feature counter-propagating edge modes crossing the zero energy at  $k_y = 0$  ( $\pm\pi/a$ ), when the underlying QSHI is in the  $\Gamma$  ( $M$ ) phase. On the other hand, the middle layer is devoid of any chiral edge state. Surface localized chiral edge states also manifest

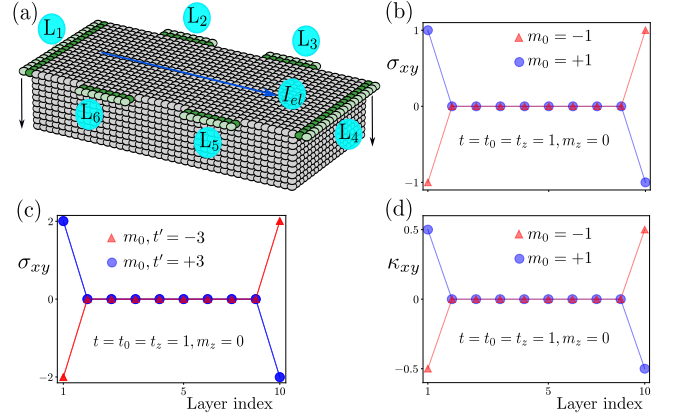


FIG. 4. (a) Six-terminal setup for the layer-resolved Hall conductivity. (b) Layer-resolved electrical Hall conductivity ( $\sigma_{xy}$ ) for HSCTI, showing its integer quantization (in units of  $e^2/h$ ) on the top and bottom surfaces with opposite signs. (c) Same as (b), but for crystalline HSCTI with a parent QSHI featuring band inversion at the X and Y points of a 2D BZ. (d) Thermal Hall conductivity ( $\kappa_{xy}$ ) for thermal HSCTI (superconductor), showing its half-integer quantization (in units of  $\kappa_0 = \pi^2 k_B^2 T / (3h)$ ) at temperature  $T = 0.01$  only the top and bottom surfaces with opposite signs.

through the layer-resolved integer quantized charge Hall conductivity ( $\sigma_{xy}$ ), which we discuss next.

*Hall effect.* To compute the layer-resolved Hall conductivity in a 3D HSCTI, we consider a six-terminal Hall bar geometry. See Fig. 4(a). All the voltage and current leads are one-layer thick. An electrical current  $I_{\text{el}}$  is passed between the leads  $L_1$  and  $L_4$ . Then a transverse or Hall voltage develops between the leads  $L_2$  and  $L_6$ , and  $L_3$  and  $L_5$ . We numerically compute the Hall resistance  $R_{xy}^{\text{el}} = (V_2 + V_3 - V_5 - V_6) / (2I_{\text{el}})$  using Kwant by attaching all the leads to a specific layer [43, 44]. Here  $V_j$  is the voltage at the  $j$ th lead ( $L_j$ ). The Hall conductivity is given by  $\sigma_{xy} = (e^2/h) (R_{xy}^{\text{el}})^{-1}$ . The results are shown in Fig. 4(b). It shows that  $\sigma_{xy}$  is quantized (in units of  $e^2/h$ ) on the top and bottom surfaces, where they have opposite signs. It can be anchored by computing the first Chern number ( $C$ ) of the surface Hamiltonian [Eq. (4)] as  $\sigma_{xy} = Ce^2/h$ . On any other layer  $\sigma_{xy} = 0$ . The overall sign of  $\sigma_{xy}$  flips between the  $\Gamma$  and  $M$  phases of the parent QSHI. Additional details of this computation are presented in the Supplemental Material [33].

*Topological invariant.* At the TRIM points  $d_1(\mathbf{k}) = d_2(\mathbf{k}) = d_4(\mathbf{k}) = 0$ , and  $h_{\text{HSCTI}}^{\text{3D}} = \Gamma_3 d_3(\mathbf{k}) + \Gamma_5 d_5(\mathbf{k})$  can be brought into a block diagonal form after a suitable unitary rotation with  $\Gamma_4 = \sigma_3 \tau_1$  and  $\Gamma_5 = \sigma_3 \tau_2$ . We then define a quantity  $\hat{\phi}_{\mathbf{k}} = \phi_{\mathbf{k}} / |\phi_{\mathbf{k}}|$ , where  $\phi_{\mathbf{k}} = \tan^{-1}[d_5(\mathbf{k})/d_3(\mathbf{k})]$ . By construction,  $\hat{\phi}_{\mathbf{k}} = \pm 1$ . The system then describes a TI only when

$$\Phi_z = \hat{\phi}_{j,k_{z,1}}^* \hat{\phi}_{j,k_{z,2}}^* = -1 \text{ and } \Phi_{xy} = \prod_j \hat{\phi}_{j,k_{z,i}}^* = -1, \quad (5)$$

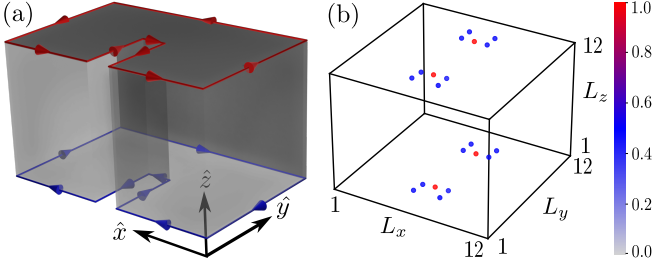


FIG. 5. (a) A  $z$ -directional Volterra cut of a line of atoms in a 3D HSCTI crystal that creates new edges on  $xy$  plane, supporting counter-propagating chiral edge modes only on the top and bottom surfaces. When these edges are pasted to create a line of edge dislocations, the edge modes hybridize and produce zero energy surface bound defect modes when the parent QSHI is in the M phase, for example. (b) Normalized local density of states for such defect modes with a edge (anti)dislocation pair and periodic boundary conditions in the  $x$  and  $y$  directions, for  $m_0/t_0 = 1$  and  $m_z/t_z = 0$ .

for  $i = 1$  and  $2$ , where  $\mathbf{k}_z^* = (0, \pi/a)$ ,  $j = \Gamma, M, X, Y$  are the TRIM points of a 2D BZ with  $X = (1, 0)\pi/a$  and  $Y = (0, 1)\pi/a$ . When  $\Phi_z = -1$ , the  $z$ -directional SSHI features band inversion along  $k_z$  at all the TRIM points on the 2D BZ. On the other hand, when  $\Phi_{xy} = -1$  the planar QSHI features band inversion at odd number of TRIM points on the 2D BZ for  $k_z = 0$  and  $\pi/a$ . The TRIM band inversion point of the 2D BZ can be identified from the Pfaffian invariant [6]. On the other hand, if  $\Phi_z$  or  $\Phi_{xy}$  becomes  $+1$ , the system is a trivial insulator or crystalline HSCTI, which we discuss next.

**Crystalline HSCTI.** With  $d_1(\mathbf{k}) = S_x + C_x S_y$ ,  $d_2(\mathbf{k}) = S_y + S_x C_y$  and  $d_3(\mathbf{k}) = m_0 - 2t' + t_0(C_x + C_y) + 2t'(C_x C_y)$ , where  $S_j = \sin(k_j a)$  and  $C_j = \cos(k_j a)$ , the band inversion occurs at the X and Y points of the 2D BZ for  $|m_0/t_0| > 2$  and  $t'/t_0 > m_0/(4t_0)$ , yielding a crystalline QSHI protected by the four-fold rotational ( $C_4$ ) symmetry [21]. The resulting HSCTI is then also protected by the  $C_4$  symmetry. The layer-resolved Hall conductivity  $\sigma_{xy} = \pm 2e^2/h$  on the top and bottom surfaces, respectively, as they host two counter-propagating chiral edge states. See Fig. 3(c). In this phase  $\Phi_{xy} = +1$  as the band inversion for the QSHI occurs at an even number of TRIM points in the 2D BZ. But, the Pfaffian at the X and Y points are  $-1$ , protected by the  $C_4$  symmetry [21].

**Lattice defects.** When the band inversion of the underlying QSHI occurs at a finite TRIM point ( $\mathbf{K}_{\text{inv}}^{\text{QSHI}}$ ), the 3D HSCTI becomes translationally active. Dislocation lattice defects, created by breaking the local translational symmetry in the bulk of a crystal, are instrumental to identify them in terms of topological modes bound to their cores. A screw dislocation fosters gapless modes only when the associated Burgers vector ( $\mathbf{b}$ ) pierces gapless surfaces [45–47]. As all the surfaces of a 3D HSCTI are gapped, screw dislocations do not host any metallic

defect modes. A line of edge dislocation is characterized by  $\mathbf{b}$  and the stacking direction ( $\hat{\mathbf{s}}$ ). Only when  $\hat{\mathbf{s}} = \hat{\mathbf{z}}$  and  $\mathbf{b} = a\hat{\mathbf{x}}$  or  $a\hat{\mathbf{y}}$ , the Burgers vector points toward gapless chiral edge states on the top and bottom surfaces. Once a line of atoms is removed, counter-propagating chiral edge states appear at the newly created edges on these two surfaces. See Fig. 5(a). Upon reconnecting these edges a 3D edge dislocation is created through the Volterra cut-and-paste procedure, and the edge modes hybridize. When  $\mathbf{K}_{\text{inv}}^{\text{QSHI}} \cdot \mathbf{b} = \pi$  (modulo  $2\pi$ ) [41, 45–52], as is the case when the QSHI resides in the M or XY phase, the nontrivial  $\pi$  hopping phase around the defect core binds surface localized zero energy modes. See Fig. 5(b).

**Superconductivity.** With a suitable  $\Gamma$  matrix representation,  $h_{\text{HSCTI}}^{\text{3D}}$  can describe a hybrid symmetry class topological superconductor. For example, when  $\Gamma_1 = \eta_1 \sigma_0$ ,  $\Gamma_2 = \eta_2 \sigma_3$  and  $\Gamma_3 = \eta_3 \sigma_0$ , where the set of Pauli matrices  $\{\eta_\mu\}$  operates on the Nambu or particle-hole indices,  $H_{\text{QSHI}}^{\text{xy}}$  describes a  $p_x \pm ip_y$  paired state (class DIII), occupying the  $xy$  plane and stacked in the  $z$  direction. Now  $t$  represents the pairing amplitude and  $d_3(\mathbf{k})$  gives rise to a cylindrical Fermi surface when  $|m_0/t_0| < 2$ . In this basis  $H_{\text{SSHI}}^z$  describes a  $z$ -directional Kitaev chain of Majorana Fermions (class D or BDI) that couples the layers of  $p_x \pm ip_y$  superconductors. Physically,  $d_4(\mathbf{k})$  ( $d_5(\mathbf{k})$ ) describes a  $p_z$ -wave ( $\mathcal{PT}$  symmetry breaking extended  $s$ -wave) pairing for  $\Gamma_4 = \eta_2 \sigma_1$  and  $\Gamma_5 = \eta_2 \sigma_2$ .

On the top and bottom surfaces, such a topological paired state supports 2D thermal Hall insulators of opposite Chern numbers. Their edge modes are constituted by counter propagating chiral Majorana fermions on opposite surfaces, each of which yields a half-quantized thermal Hall conductivity ( $\kappa_{xy}$ ) in units of  $\kappa_0$  at small temperature ( $T \rightarrow 0$ ), where  $\kappa_0 = \pi^2 k_B^2 T / (3h)$ . Layer resolved numerical computation of  $\kappa_{xy}$  in the six-terminal Hall bar geometry confirms this outcome and shows that it is indeed of opposite signs on the top and bottom surfaces. See Fig. 4(d). Details of this computation is shown in the Supplemental Material [33]. The edge dislocations with  $\mathbf{b} = a\hat{\mathbf{x}}$  or  $a\hat{\mathbf{y}}$  and  $\hat{\mathbf{s}} = \hat{\mathbf{z}}$ , in such a paired state support surface localized endpoint Majorana modes.

**Discussions & outlooks.** We outline a general principle of realizing HSCTIs from two distinct parent TIs that occupy orthogonal Cartesian hyperplanes and belong to different AZSCs. Explicitly discussed HSCTI, obtained via a hybridization between  $xy$  planar QSHIs (class AII) and  $z$ -directional SSHIs (class BDI), possesses a bulk topological invariant and manifests bulk-boundary correspondence by harboring surface QAHIs (class A), leaving its fingerprint on chiral edge states and layer-resolved quantized Hall effect. Our proposal thereby offers a unique approach to vision TIs at the boundaries of an even higher-dimensional HSCTI. For example, following the same principle a 3D class AII TI can be found on the boundary of a four-dimensional HSCTI, built from 3D class CII and 1D class BDI TIs, which we show in the Sup-

plemental Material [33]. This route is distinct from the “dimensional reduction” of constructing a  $d$ -dimensional TI from a fixed AZSC  $d+1$ -dimensional one [53]. We also extend the jurisdiction of this proposal to systems, where at least one of the constituting parent TIs is protected by crystalline symmetry and to encompass superconducting states, featuring half-quantized surface thermal Hall conductivity. Existence of a plethora of strong and crystalline topological phases of matter (insulators and superconductors) of various dimensions and symmetries in nature [1–28] should therefore open an unexplored territory of HSCTIs (electrical and thermal) that in principle can be realized in quantum crystals and engineered in classical metamaterials.

As  $d_5(\mathbf{k})$  breaks both  $\mathcal{P}$  and  $\mathcal{T}$  symmetries, layered magnetic materials with columnar antiferromagnetic order in the stacking direction constitute an ideal platform to harness the candidate 3D HSCTI. With the recent discovery of (anti)ferromagnetic TI  $\text{MnBi}_2\text{Te}_4$  [54–57] (possibly axionic), we are optimistic that HSCTI can be found in some available or newly synthesized quantum materials using the existing vast dictionary of magnetic materials [58], guided by topological quantum chemistry [24–27]. When such materials (once found) are doped, they can harbor thermal HSCTI or superconductors from local or on-site pairings, as by now it is well established that the local paired states often (if not always) inherit topology from parent normal state electronic bands, even when it is a trivial insulator in the presence of a Fermi surface, but in terms of neutral Majorana fermions [59–63]. We leave this topic for a future investigation.

As the model Hamiltonian for HSCTI is described in terms of only nearest-neighbor hopping amplitudes, it can be emulated in classical metamaterials, among which topoelectric circuits [64–66] and mechanical lattices [67–69] are the two most prominent ones. In both setups existence of chiral edge modes of 2D TIs has been experimentally demonstrated from the unidirectional propagation of a weak (low energy) disturbance only along their edges [65, 67–69]. Finally, we note that topological defect modes have been experimentally observed in quantum crystals [70–72] and mechanical lattices [73]. Thus, our predicted counter-propagating chiral edge modes on the opposite surfaces of the 3D HSCTI and surface localized dislocation bound states should be within the reach of currently available experimental facilities.

*Acknowledgments.* S.K.D. was supported by a Startup grant of B.R. from Lehigh University. B.R. was supported by NSF CAREER Grant No. DMR- 2238679. We thank Daniel J. Salib for useful discussion.

---

[1] M. Z. Hasan and C. L. Kane, Rev. Mod. Phys. **82**, 3045 (2010).

[2] X.-L. Qi and S. C. Zhang, Rev. Mod. Phys. **83**, 1057 (2011).

[3] C.-K. Chiu, J. C. Y. Teo, A. P. Schnyder, and S. Ryu, Rev. Mod. Phys. **88**, 035005 (2016).

[4] C. L. Kane and E. J. Mele, Phys. Rev. Lett. **95**, 146802 (2005).

[5] B. A. Bernevig, T. L. Hughes, and S.-C. Zhang, Science **314**, 1757 (2006).

[6] L. Fu and C. L. Kane, Phys. Rev. B **76**, 045302 (2007).

[7] M. König, S. Wiedmann, C. Brüne, A. Roth, H. Buhmann, L. W. Molenkamp, X.-L. Qi, and S.-C. Zhang, Science **318**, 766 (2007).

[8] D. Hsieh, D. Qian, L. Wray, Y. Xia, Y. S. Hor, R. J. Cava, and M. Z. Hasan, Nature (London) **452**, 970 (2008).

[9] H. Zhang, C.-X. Liu, X.-L. Qi, X. Dai, Z. Fang, and S.-C. Zhang, Nat. Phys. **5**, 438 (2009).

[10] Y. L. Chen, J. G. Analytis, J.-H. Chu, Z. K. Liu, S.-K. Mo, X. L. Qi, H. J. Zhang, D. H. Lu, X. Dai, Z. Fang, S. C. Zhang, I. R. Fisher, Z. Hussain, and Z.-X. Shen, Science **325**, 178 (2009).

[11] K. v. Klitzing, G. Dorda, and M. Pepper, Phys. Rev. Lett. **45**, 494 (1980).

[12] D. J. Thouless, M. Kohmoto, M. P. Nightingale, and M. den Nijs, Phys. Rev. Lett. **49**, 405 (1982).

[13] F. D. M. Haldane, Phys. Rev. Lett. **61**, 2015 (1988).

[14] A. Altland and M. R. Zirnbauer, Phys. Rev. B **55**, 1142 (1997).

[15] A. P. Schnyder, S. Ryu, A. Furusaki, and A. W. W. Ludwig, Phys. Rev. B **78**, 195125 (2008).

[16] S. Ryu, A. Schnyder, A. Furusaki, and A. Ludwig, New J. Phys. **12**, 065010 (2010).

[17] G. E. Volovik, The Universe in a Helium Droplet (Oxford University Press, 1st ed., 2003).

[18] Y. Ando and L. Fu, Annu. Rev. Condens. Matter Phys. **6**, 361 (2015).

[19] M. Sato and Yoichi Ando, Rep. Prog. Phys. **80**, 076501 (2017).

[20] L. Fu, Phys. Rev. Lett. **106**, 106802 (2011).

[21] R.-J. Slager, A. Mesaros, V. Juričić, and J. Zaanen, Nat. Phys. **9**, 98 (2013).

[22] K. Shiozaki and M. Sato, Phys. Rev. B **90**, 165114 (2014).

[23] J. Kruthoff, J. de Boer, J. van Wezel, C. L. Kane, and R.-J. Slager, Phys. Rev. X **7**, 041069 (2017).

[24] B. Bradlyn, L. Elcoro, J. Cano, M. G. Vergniory, Z. Wang, C. Felser, M. I. Aroyo, and B. A. Bernevig, Nature (London) **547**, 298 (2017).

[25] T. Zhang, Y. Jiang, Z. Song, H. Huang, Y. He, Z. Fang, H. Weng, and C. Fang, Nature (London) **566**, 475 (2019).

[26] M. G. Vergniory, L. Elcoro, C. Felser, N. Regnault, B. A. Bernevig, and Z. Wang, Nature (London) **566**, 480 (2019).

[27] F. Tang, H. C. Po, A. Vishwanath, and X. Wang, Nature (London) **566**, 486 (2019).

[28] S. K. Das, B. Yan, J. van den Brink, and I. C. Fulga, Phys. Rev. B **99**, 165418 (2019).

[29] C.-X. Liu, X.-L. Qi, H.-J. Zhang, X. Dai, Z. Fang, and S.-C. Zhang, Phys. Rev. B **82**, 045122 (2010).

[30] F. Schindler, A. M. Cook, M. G. Vergniory, Z. Wang, S. S. P. Parkin, B. A. Bernevig, and T. Neupert, Sci. Adv. **4**, eaat0346 (2018).

[31] W. A. Benalcazar, B. A. Bernevig, and T. L. Hughes, Science **357**, 61 (2017).

[32] T. Nag, V. Juričić and B. Roy, Phys. Rev. B **103**, 115308 (2021).

- [33] See Supplemental Material for additional results.
- [34] A. M. Essin, J. E. Moore, and D. Vanderbilt, *Phys. Rev. Lett.* **102**, 146805 (2009).
- [35] R. Li, J. Wang, X-L. Qi, and S-C. Zhang, *Nat. Phys.* **6**, 284 (2010).
- [36] B. Roy, P. Goswami, and J. D. Sau, *Phys. Rev. B* **94**, 041101 (2016).
- [37] W. P. Su, J. R. Schrieffer, and A. J. Heeger, *Phys. Rev. Lett.* **42**, 1698 (1979).
- [38] W. P. Su, J. R. Schrieffer, and A. J. Heeger, *Phys. Rev. B* **22**, 2099 (1980).
- [39] A. J. Heeger, S. Kivelson, J. R. Schrieffer, and W.-P. Su, *Rev. Mod. Phys.* **60**, 781 (1988).
- [40] B. Roy, *Phys. Rev. Res.* **1**, 032048(R) (2019).
- [41] V. Juričić, A. Mesaros, R.-J. Slager, and J. Zaanen, *Phys. Rev. Lett.* **108**, 106403 (2012).
- [42] X-L. Qi, Y.-S. Wu, and S-C. Zhang, *Phys. Rev. B* **74**, 085308 (2006).
- [43] C. W. Groth, M. Wimmer, A. R. Akhmerov, and X. Waintal, *New J. Phys.* **16**, 063065 (2014).
- [44] S. K. Das, S. Manna, and B. Roy, *arXiv:2211.09804*
- [45] Y. Ran, Y. Zhang, and A. Vishwanath, *Nat. Phys.* **5**, 298 (2009).
- [46] R.-J. Slager, A. Mesaros, V. Juričić, and J. Zaanen, *Phys. Rev. B* **90**, 241403(R) (2014).
- [47] B. Roy and V. Juričić, *Phys. Rev. Res.* **3**, 033107 (2021).
- [48] J. C. Y. Teo and C. L. Kane, *Phys. Rev. B* **82**, 115120 (2010).
- [49] D. Asahi and N. Nagaosa, *Phys. Rev. B* **86**, 100504(R) (2012).
- [50] T. L. Hughes, H. Yao, and X.-L. Qi, *Phys. Rev. B* **90**, 235123 (2014).
- [51] T. Nag and B. Roy, *Commun. Phys.* **4**, 157 (2021).
- [52] A. Panigrahi, R. Moessner, and B. Roy, *Phys. Rev. B* **106**, L041302 (2022).
- [53] X-L. Qi, T. L. Hughes, and S-C. Zhang, *Phys. Rev. B* **78**, 195424 (2008).
- [54] J. Li, Y. Li, S. Du, Z. Wang, B-L. Gu, S-C. Zhang, K. He, W. Duan, and Y. Xu, *Sci. Adv.* **5**, eaaw5685 (2019).
- [55] C. Liu, Y. Wang, H. Li, Y. Wu, Y. Li, J. Li, K. He, Y. Xu, J. Zhang, and Y. Wang, *Nat. Mater.* **19**, 522 (2020).
- [56] M. Gu, J. Li, H. Sun, Y. Zhao, C. Liu, J. Liu, H. Lu, and Q. Liu, *Nat Commun* **12**, 3524 (2021).
- [57] W. Lin, Y. Feng, Y. Wang, J. Zhu, Z. Lian, H. Zhang, H. Li, Y. Wu, C. Liu, Y. Wang, J. Zhang, Y. Wang, C-Z. Chen, X. Zhou, and J. Shen, *Nat Commun* **13**, 7714 (2022).
- [58] *Handbook of Magnetic Materials* (Elsevier, North Holland, 2022), Vol. 1-31.
- [59] L. Fu and E. Berg, *Phys. Rev. Lett.* **105**, 097001 (2010).
- [60] L. Fu, *Phys. Rev. B* **90**, 100509(R) (2014).
- [61] B. Roy, Y. Alavirad, and J. D. Sau, *Phys. Rev. Lett.* **118**, 227002 (2017).
- [62] B. Roy, *Phys. Rev. B* **101**, 220506(R) (2020).
- [63] B. Roy and V. Juričić, *Phys. Rev. B* **104**, L180503 (2021).
- [64] C. H. Lee, S. Imhof, C. Berger, F. Bayer, J. Brehm, L. W. Molenkamp, T. Kiessling, and R. Thomale, *Commun. Phys.* **1**, 39 (2018).
- [65] T. Hofmann, T. Helbig, C. H. Lee, M. Greiter, and R. Thomale, *Phys. Rev. Lett.* **122**, 247702 (2019).
- [66] J.-K. Dong, V. Juričić, and B. Roy, *Phys. Rev. Res.* **3**, 023056 (2021).
- [67] R. Süssstrunk and S. D. Huber, *Science* **349**, 47 (2015).
- [68] Z. Yang, F. Gao, X. Shi, X. Lin, Z. Gao, Y. Chong, and Baile Zhang, *Phys. Rev. Lett.* **114**, 114301 (2015).
- [69] C. He, X. Ni, H. Ge, X.-C. Sun, Y.-B. Chen, M.-H. Lu, X.-P. Liu, and Y.-F. Chen, *Nat. Phys.* **12**, 1124 (2016).
- [70] A. K. Nayak, J. Reiner, R. Queiroz, H. Fu, C. Shekhar, B. Yan, C. Felser, N. Avraham, and H. Beidenkopf, *Sci. Adv.* **5**, eaax6996 (2019).
- [71] H. Hamasaki, Y. Tokumoto, and K. Edagawa, *Appl. Phys. Lett.* **110**, 092105 (2017).
- [72] H. W. Kim, S-H. Kang, H-J. Kim, K. Chae, S. Cho, W. Ko, S. H. Kang, H. Yang, S. W. Kim, S. Park, S. W. Hwang, Y-K. Kwon, Y-W. Son, *Nano Lett.* **20**, 5837 (2020).
- [73] I. H. Grinberg, M. Lin, W. A. Benalcazar, T. L. Hughes, and G. Bahl, *Phys. Rev. Applied* **14**, 064042 (2020).